WILEY-VCH

Tunable microwave conductance of nanodomains in ferroelectric $PbZr_{0.2}Ti_{0.8}O_3$ thin film

Stuart R. Burns, Alexander Tselev, Anton V. Ievlev, Joshua C. Agar, Lane W. Martin, Sergei V. Kalinin, Daniel Sando, Petro Maksymovych**

Dr. S.R. Burns, Dr. D. Sando
School of Materials Science and Engineering, University of New South Wales, Sydney 2052, Australia

Dr. S.R. Burns,
Department of Chemistry, University of Calgary, Calgary AB T2N 1N4, Canada
E-mail: stuart.burns@ucalgary.ca

Dr. A. Tselev,
CICECO-Aveiro Institute of Materials and Department of Physics, University of Aveiro, 3810-193 Aveiro, Portugal

Dr A.V. Ievlev, Dr S.V. Kalinin, Dr P. Maksymovych,
Centre for Nanophase Materials Sciences, Oak Ridge National Laboratory, Oak Ridge, TN 37831, USA
Email: maksymovychp@ornl.gov

Asst. Prof. J.C. Agar, Prof. L.W. Martin,
Department of Materials Science and Engineering, University of California, Berkeley, Berkeley CA 94720, USA

Asst. Prof. J.C. Agar,
Department of Material Science and Engineering, Lehigh University, Bethlehem, Pennsylvania 18015, USA

Prof. L.W. Martin,
Materials Sciences Division, Lawrence Berkeley National Laboratory, Berkeley, CA 94720, USA

Keywords: lead zirconate titanate, thin film, scanning probe microscopy, domain wall conductance, scanning microwave impedance microscopy

Ferroelectric materials exhibit spontaneous polarization that can be switched by electric field. Beyond traditional applications as non-volatile capacitive elements, the interplay between polarization and electronic transport in ferroelectric thin films has enabled a path to neuromorphic device applications involving resistive switching. A fundamental challenge, however, is that finite electronic conductivity may introduce considerable power dissipation and perhaps destabilize ferroelectricity itself. Here, we reveal tunable microwave frequency

electronic response of domain walls injected into ferroelectric lead zirconate titanate ($PbZr_{0.2}Ti_{0.8}O_3$, PZT) on the level of a single nanodomain. We detected tunable microwave response through first-order reversal curve spectroscopy combined with scanning microwave impedance microscopy (sMIM) measurements taken near 3 GHz. We have investigated contributions of film interfaces to the measured ac conduction through subtractive milling, where the film exhibited improved conduction properties after removal of surface layers. Using statistical analysis and finite element modelling, we inferred that the mechanism of tunable microwave conductance is the variable area of the domain wall in the switching volume. These observations open the possibilities for ferroelectric memristors or volatile resistive switches, localized to several tens of nanometres and operating according to well-defined dynamics under an applied field.

1. Introduction

Ferroelectric materials have long been pursued for use in non-volatile memory and logic applications. Polarization switching has been employed in capacitive ferroelectric memories, where information is stored in the polarization orientation. A recent resurgence of interest in electronic properties of ferroelectrics, such as polarization controlled tunneling and conductivity of domain walls, potentially enables a new generation of applications utilizing resistive probes of polarization state, such as synaptic junctions (FTJs), [1–5] domain-wall resistors, and domain-wall logic. [6–9] At the same time, ferroelectric control over resistive switching may enable neuromorphic devices without structural phase change and filamentary breakdown, potentially leading to much higher energy efficiency.

One of the key properties enabling the coupling of ferroelectric and resistive switching is the electronic conductivity of domain walls, [10] which was experimentally demonstrated in numerous materials, [11–14] beginning with the work of Seidel *et al.*. [15] The intrinsic

coupling of domain walls to applied electric field, their nanoscale dimensions and the flexibility afforded by deterministic control of ferroelectric, ferroelastic, and ferromagnetic structures containing conducting domain walls [16–20] provide great promise for new memory and electronics-engineering concepts, such as racetrack memories [21] or magnetoelectric spin-orbit (MESO) devices. [22] A notable challenge on the path of ferro-resistive switching is that metallic conductivity and ferroelectricity are fundamentally opposed. [23,24] In turn, it is highly non-trivial to establish good electrical contact to the domain wall. [25] In fact, charged domain walls may reconstruct in the contact region preventing good metallic contact from being established on an intrinsic level. [26] The other fundamental issue is that domain-wall conductivity increases with increasing charge of the domain wall, but so does the domain-wall energy, [27] which ultimately requires unique approaches to creating strongly conductive domain walls. Meanwhile, increasing carrier density in the bulk by doping/alloying is also complicated and may eventually suppress ferroelectric ordering. [28]

An alternative regime to measure electronic properties of ferroelectric domain walls relies on high-frequency ac regimes. [29] High-frequency ac conductance effectively shorts the Schottky barrier, making highly resistive contacts required for ferroelectric switching compatible with an electronic read-out of the ferroelectric state. [30,31] This mechanism is complementary to a recently demonstrated photovoltaic read-out of the ferroelectric state, which likewise circumvents the need for Ohmic contacts. [32]

Here, we report the observation of tunable electronic properties of ferroelectric switching at microwave frequencies and on the level of a single ferroelectric nanodomain. Utilizing a scanning probe as a top electrode, we locally switched the domain structure of a thin $PbZr_{0.2}Ti_{0.8}O_3$ (PZT) film. [33,34] Through a combination of first-order reversal curve (FORC) spectroscopy, which creates nanodomains in sub-100 nm regions of the ferroelectric film and probes their evolution, and simultaneous piezoresponse force (PFM) and microwave

(sMIM) measurements, we captured the evolution and dynamics of the ferroelectric state. The results reveal tunable microwave conductance states encoded by the wall's size and effective density under the probe tip. These results point to memristive behavior from a single ferroelectric nanodomain and are supported by finite-element simulations based upon Landau-Ginzburg-Devonshire (LGD) theory. Furthermore, subtractive lithography [35] was applied to probe the sensitivity of tunable microwave conductance in relation to film thickness of the ferroelectric, finding enhancement of microwave conductance in the desired ultrathin limit. Tunable microwave conductance defined by effective domain-wall density may facilitate the realization of ferroelectric memristive devices at microwave frequencies that remain primarily insulating in the dc regime. Power dissipation in such devices would ideally be minimized to capacitive and dielectric effects – potentially shifting the switching power of such devices into the femto- or even atto-joule regime. [36] At the same time, the microwave probe provides new nanoscale insights into the ferroelectric-switching process, extending previous observations of microwave domain-wall conductance [29,30,37] to ferroelectric dynamics in an electric field.

2. Results and Discussion

Simultaneous sMIM and PFM spectroscopies were carried out while locally switching domains using an applied electric field. **Figure 1a** shows a generic scenario for domain-wall nucleation and local switching under the nanoscale probe. The conductive AFM probe acts as the top electrode in a capacitor geometry. Above a critical electric field, the polarization begins to switch directly under the probe. The colors show the evolution of the polarization nanodomain as a function of time, showing its progressive growth through the depth of the film (perpendicular growth), and eventually, the expanding domain sidewalls (lateral growth) toward formation of a cylindrical domain.

The system under study is presented schematically in **Figure 1b.** The $PbZr_{0.2}Ti_{0.8}O_3$ /$SrRuO_3$/$SrTiO_3$ (001) (PZT/SRO/STO) heterostructure (Methods) is characterized by a shielded sMIM probe in contact with the top surface. The sMIM probe acts as a lumped element terminating a half-wave resonator. sMIM data are collected from two decoupled signal channels, namely sMIM-G (conductance) and sMIM-C (susceptance or capacitance). Preliminary testing to separate the contribution of applied biases – ac low-frequency (driving PFM, on the order of kHz), ac high-frequency (driving sMIM, on the order of GHz), and dc (driving the local domain switching) – indicated that the corresponding spectra did not suffer from cross-coupling with other probing potentials. Further details on the sMIM apparatus and similar experimental configurations can be found elsewhere [30,38,39].

FORC switching spectroscopy was applied to probe the switching scenario and track the growing nanodomains' properties in the microwave regime. The distinctive trait of the FORC waveform is the iteratively changing negative bias limit with each cycle, which we refer to as the turning bias, V_{turn}, highlighted by the dot marker on the waveform in **Figure 1c**. This waveform probes nanodomains in the three regimes of the switching process: prior to, during, and following the coercive field being reached by applied dc bias.

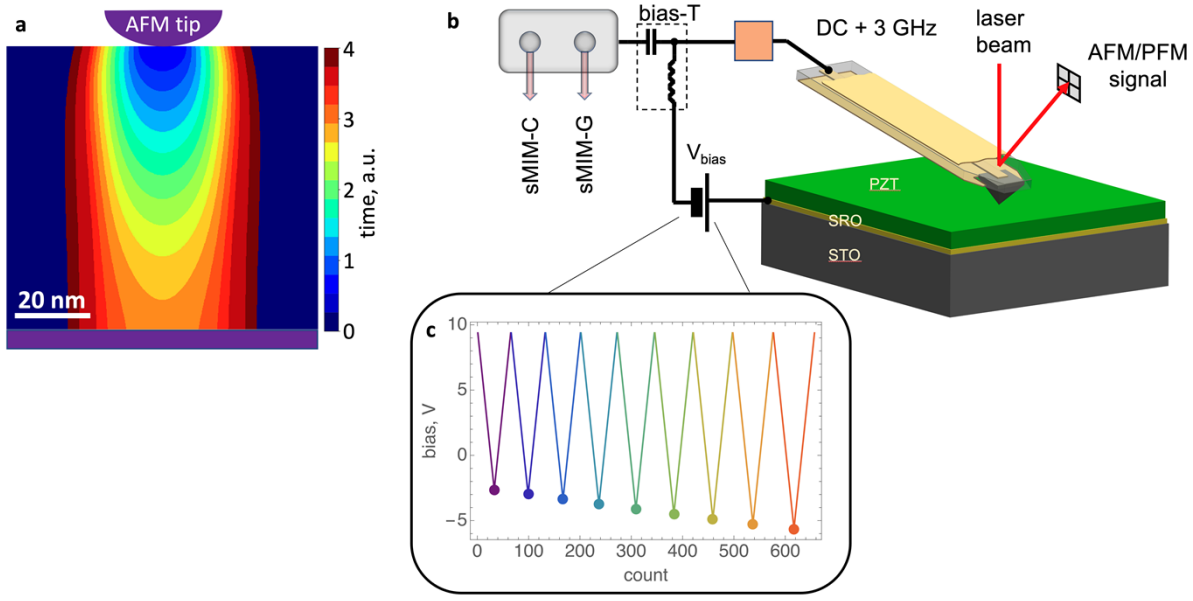

Figure 1. Schematic of the measurement of tunable microwave conductance of ferroelectric domain walls. **a)** Nucleation and growth of a single nanodomain in localized electric field of a nanoscale capacitor. Colors identify the shape of the nanodomain cross-section calculated as a function of time following nucleation. The domain wall of the nanodomain immediately following nucleation assumes the shape of a prolate half-spheroid. As the domain grows, the spheroid continues to elongate, eventually traversing the film thickness to become cylindrical. **b)** Schematic of a scanning microwave measurement set-up used to characterize nanodomains. A voltage-biased shielded probe terminating a half-wave resonator is used to apply a local electric field to a thin PZT ferroelectric film and to probe ferroelectric properties through the amplitude and phase of the microwaves reflected from the probe. The latter are translated into variations of capacitance (sMIM-C) and conductance (sMIM-G) of the probe-sample system by accompanying system calibration. **c)** The probe voltage bias waveform implements a first order reversal curve (FORC) measurement, wherein the system state is probed as a function of increasing turning voltage (V_{turn} - marked by a dot) in a sequence of linear voltage sweeps. The range of V_{turn} is chosen to precede, coincide and exceed the switching voltage for the ferroelectric polarization in the film, thereby probing single (or few) nanodomains nucleating and growing under the probe.

PFM and sMIM FORC spectroscopy results (collected simultaneously) are presented in **Figure 2**. Minor hysteresis loops along the FORC are observed in both sMIM (**Figure 2a,b)** and PFM channels (**Figure 2c)**. The ferroelectric switching is initiated in the approximate window from -2.5V ~ - 3.5 V depending on specific location on the surface. The switching processes is detected by rapid variation of all the measured signals in **Figure 2**. However, each signal reveals its own characteristic trend. Both capacitance and conductance achieves peak value at the forward and the reverse switching events (Fig. 2a,b). However, they are different with respect to the bias change around the switching events. The capacitance shows little remnance around 0V, regardless of the specific value of V_{turn}. In other words, it doesn't have a strong memory of the degree of switching. In contrast, conductance reveals a series of plateaus between the switching events (Fig. 2b), whose value strongly depends on V_{turn} (Fig 2b and Fig 2d). This observation suggests that with even finer bias increments a potentially quasi-continuous multilevel conductance states can be read-out from a single switching event. **Figure 2c** clearly points to the ferroelectric origin of the metastable states responsible for tunable conductance, since they emerge during partial ferroelectric switching. We have not yet explored the temporal stability of these states. Given the timescale of the experiment, the states have a lifetime of at least a few seconds. Larger domains nucleated under the tip shown below are stable on much longer timescales in this film. Finally, **Figure 2d** confirms the repeatability of these results – each point at a given V_{turn} value corresponds to a set of data collected in a different region of the PZT film. The contour plot superimposed on these data points was calculated by a kernel mixture distribution fit, describing the confidence of the conductance signal at a given V_{turn} bias. Given the relatively limited sampling, the finer structure of the distribution (e.g. the "blob" feature between -2 V and -3 V) is of no significance yet. However, the overall strong dependence of microwave conductance (measured at zero DC bias) on V_{turn} is statistically reproducible.

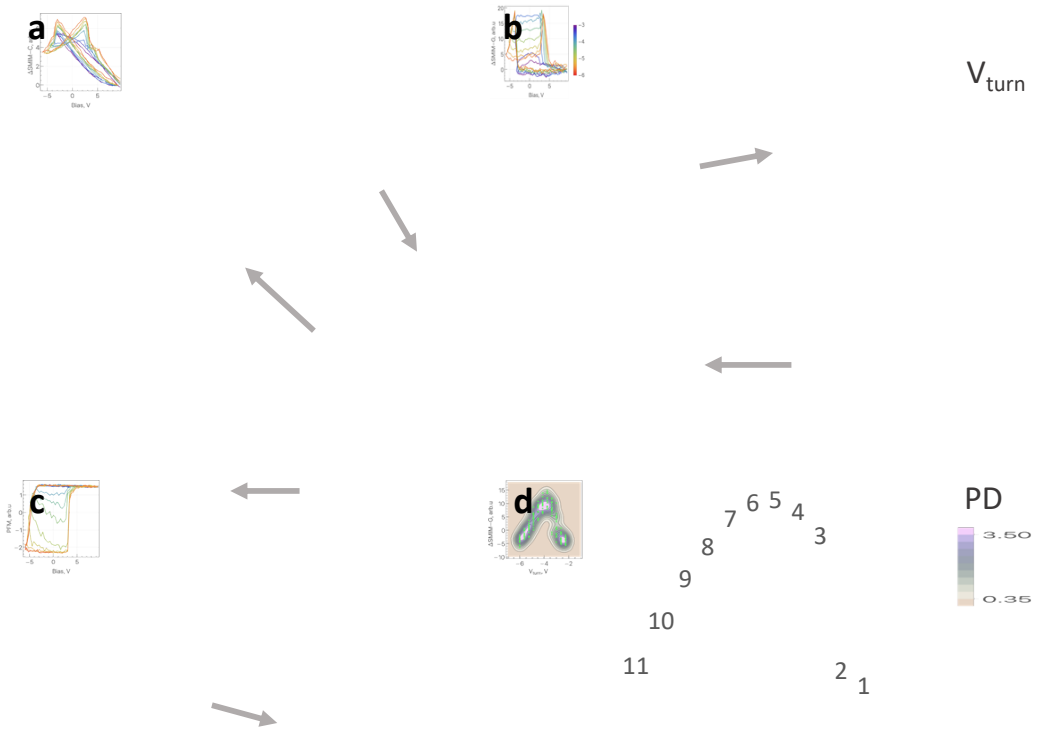

Figure 2. Observation of tunable microwave conductance of ferroelectric nanodomains. First-order reversal measurements for **a)** microwave capacitance (sMIM-C), **b)** microwave conductance (sMIM-G), and **c)** piezoresponse. The arrows point to the direction of voltage cycles. All three signals register onset of ferroelectric switching at a bias of ~-3.5 V. The sMIM-C signal is dominated by the tunability of the dielectric constant, whereas sMIM-G reveals tunable microwave conductance. The value of the microwave conductance rapidly increases immediately following switching (at -3.5 V) and then begins to revert to a lower value with increasing size of the ferroelectric domain. Intriguingly, the conductance again proceeds through the maximum along the reverse-switching direction. By controlling the degree of partial switching with the turning voltage (V_{turn}) the microwave conductance at 0V can be nearly continuously tuned. The colors in **a**, **b** and **c** correspond to the turning voltages (V_{turn}), as shown in the colorbar next to **b**. **d)** Statistics accumulated from the switching

process for more than ten sequential FORC measurements. The data points (green dots) correspond to sMIM-G signal at 0V as a function of increasing magnitude of V_{turn}. The probability distribution shown as a contour plot was estimated as a mixture distribution of Gaussian kernels fit to the data-points. The standard deviation of each Gaussian was determined to be approximately 0.24, under the constraint that it includes on average 10 measured points. The distribution shows approximate confidence limits of the microwave conductance tunability and very good reproducibility of the tunability between randomly sampled locations on the surface of the PZT film. The colorbar is the probability density (PD). Panel **d** shows data collected from voltage cycles 1 through to 11 (marked next to data), whereas, for clarity, panels **a**, **b** and **c** only present cycles 3 through to 11, as the first three cycles are near identical.

To gain deeper insight into the origins of tunable microwave conductance and to probe its dependence on the structure of the film, we employed an inverse lithography approach outlined by Ievlev *et al.* [35]. Specifically, we carried out bombardment of the film with O_2^- ions to cause progressive removal of the top layers. The sputtering process is performed simultaneously with ToF-SIMS (time-of-flight secondary ion mass spectroscopy) chemical characterization to monitor the stoichiometry of the top surface layer. In addition to the reduction in thickness, this process removes (or significantly reduces the influence of) an amorphous top layer which negatively impacts the piezoelectric properties of the film [35]. **Figure 3a** displays a sMIM-G image of the PZT film milled down to 75 nm thickness (from an original 100 nm. See images for other films in Supplementary Figure S1). An arrangement of domain walls was created by applying a bias sweep at 4 x 4 points in a predetermined grid. The "doughnut" shape apparent from the sMIM-G images indicates that, at 3 GHz, the conductance of the domain walls is higher than that of the surrounding domains. sMIM-C images on the other hand do not reveal contrast from domain walls (Supplementary Figure

S2), which points to electronic origin of microwave conductance [30]. The average of the spectra collected during this applied bias (from -10 V to 10 V in a triangular waveform) are shown in **Figure 3b**. The spectra feature conductance peaks, similar to the FORC measurements in **Figure 2b**. Combined with imaging, these data show that sMIM-G conductance peaks at the polarization switching events are mainly contributed to by domain walls. By extension, tunable microwave conductance is also underpinned by the properties of ferroelectric nanodomains mediating the switching process, rather than for example motion of adsorbates. Meanwhile, the sensitivity of the effect to detailed surface conditions is not large. In fact, the average sMIM-G spectra are less noisy upon decreased thickness and exhibit larger signal (Figure 3c). It is likely that the signal improves by removing top layer, defects, or adsorbates accumulated over time in the as-grown film [40].

Figure 3c summarizes the conductance signals by comparing their corresponding distributions obtained from sMIM images and spectra. To ascertain systematic comparison of different regions of the sample, the conductance signals observed for domain walls (in sMIM-G images and sMIM-G spectra) were normalized by subtracting the values outside the domain walls in images and away from switching events in spectra (this was done on each individual measurement prior to averaging). The contributions to the sMIM-G signal are denoted by s.#, w.# and d.#, where s, w, and d represent spectra (extracted from data similar to that shown in **Figure 3b**), walls (signal extracted from domain wall regions in sMIM images similar to in **Figure 3a**), and domains (the background signal from sMIM images), respectively. The thickness of the sample in the region is denoted by #. The violin diagrams in **Figure 3c** depict the experimental distribution of the measured values, which is quite broad owing to an expected stochastic distribution of defects in the film. Notably, microwave conductance of domain walls measured by imaging (**Figure 3a**) and peak values from spectroscopy (**Figure 3b**) are comparable, with values in spectroscopy at most a factor of two larger. This observation reaffirms the conclusion that injected domain walls are the principal contributor

of tunable conductance in switching spectroscopy, as compared to impurities, surfaces, and other factors (though their influence cannot be completely ruled out). A second observation is that there is a general trend of an increase of sMIM-G signal with decreasing thickness (**Figure 3d**). If we treat the domain wall as a conductor, a basic interpretation of this result could be the domain wall acting as a conducting filament – the conductance decreases with increasing domain wall length between electrodes and is therefore notably smaller in thicker regions of the film.

Distinctly observable tunable sMIM-G conductance can emerge from several complementary phenomena. An important feature of **Figure 3b** is that the peak conductance of the nanodomain junction is observed between the point at which polarization first switches at ~ -3.5 V, and the point before it back-switches at ~ +3V, which is uniquely revealed by the FORC measurement, and echoes an earlier similar measurement using conductive AFM at dc [41]. This property not only enhances the prospects of tuning the junction by either bias polarity, but also fundamentally implies that the junction exhibits reversible ferroelectric switching properties. In particular, the configuration of the injected domain wall that maximizes conductance at negative bias polarity is first impeded by increasing negative bias but can be restored by appropriate positive polarity. The simplest picture would correspond to a polar nanodomain that first increases in dimensions and then decreases, retracting roughly to the same overall shape.

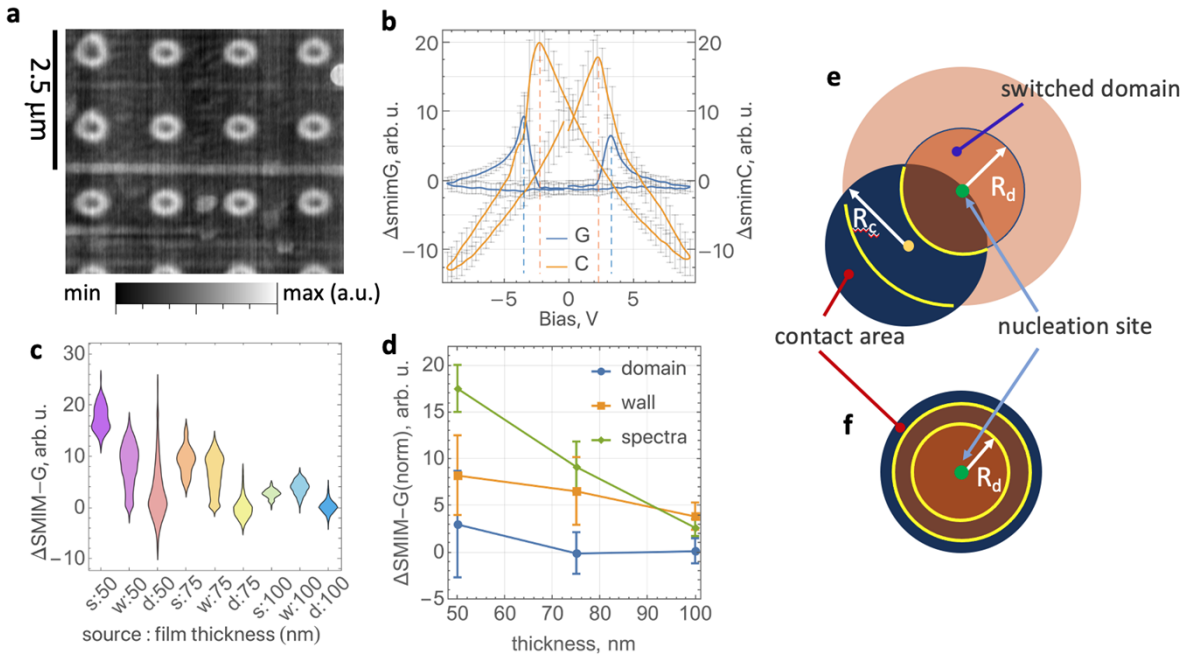

Figure 3. Microwave conductance of domain walls in PZT film with varying thicknesses. The original PZT film (native, 100 nm) was selectively sputtered by oxygen plasma (as discussed in [35]), creating regions with 75 nm and 50 nm nominal thickness. **a)** sMIM-G images of an array of nanodomains created by applying a dc pulses on a 4 x 4 point grid arrangement on the surface area of a plasma-etched 75 nm thick film. Owing to locally higher microwave conductance, the domain walls are clearly seen as "doughnut" shapes. **b)** averaged sMIM-G and sMIM-C spectra collected from the triangular bias sweep (linear voltage ramps between -10 V and +10 V), of the 50 nm thick region. The spectra show ferroelectric switching, registered as peaks in conductivity (sMIM-G) as well as dielectric constant (sMIM-C). **(c)** Statistics of thickness dependent microwave conductance of nanodomains. The "violin" diagram shows statistical distributions of the sMIM-G signals obtained by analysis of data presented in **(a,b)** from three etched areas with different thickness. The diagram compares contributions to the sMIM-G signal from domain walls measured by spectroscopy s:# (as presented in **Figure 3b**), microscopy w:# (as presented in **Figure 3a**) and the background signal away from the walls measured by microscopy d:#, where # refers to film thickness. **d)** Average values and standard deviations of the respective signals in **c)** as a function of

thickness. **e)** Schematic of the simplified geometric model of a nanodomain nucleating and growing in the contact area between the microwave probe and the ferroelectric film. The dark blue circle with the radius R_c is the tip-sample contact area; brown circle with the radius R_d and the light brown circle are a growing switched domain nucleated at the contact area boundary. The switched domain is represented by a circular cylinder for simplicity. **f)** The same as **e)** for domain nucleated at the center of the contact area.

Meanwhile, the twofold change in observed conductance can be qualitatively explained by a simple geometrical model, which considers the length of the domain wall intersecting the microwave probe's contact area. Polarization reversal is initiated somewhere in the contact region between the probe and the surface. For simplicity, we can compare two representative scenarios: nucleation in the center of the contact region and nucleation at its periphery. A schematic of the model is shown in **Figure 3e,f**. In both cases, the growth of a reversed polarization domain above the switching voltage will initially increase the length of the domain wall that intersects the contact area, and subsequently decrease it once the domain expands beyond the contact. In the nucleation at the center of the contact area, the maximum length of the domain wall in the microwave contact is $2\pi R_c$, where R_c is the contact radius. The corresponding value for the nucleation at the periphery is ~$2.24R_c$. Our reference point in **Figure 3e** is the conductance of the straight segment of the domain wall (of macroscopically large domains in **Figure 3a**) scanned by the tip. The corresponding length of the domain wall segment in that case is $2R_c$. Therefore, we expect a ratio of ~2-3 between maximum conductance observed during switching and scanning, provided the conductance of the domain wall is the same in both cases. This is indeed quite close to the experimentally observed range in **Figure 3b**, and much smaller than the one-to-three orders of magnitude change of local conductance predicted by thermodynamic modelling as a function of domain-wall tilt [42]. One possible reason is that tilted domain walls are intrinsically unstable, and

even the presence of charge compensating mechanism will quickly diminish their angle to attain lower energy configuration. It is also possible that the wall conductance observed by sMIM requires the wall to make contact to the bottom electrode. In this case, likewise, we expect to observe only a moderate tilting angle of several degrees relative to the polar axis and a correspondingly weakly charged domain wall [30].

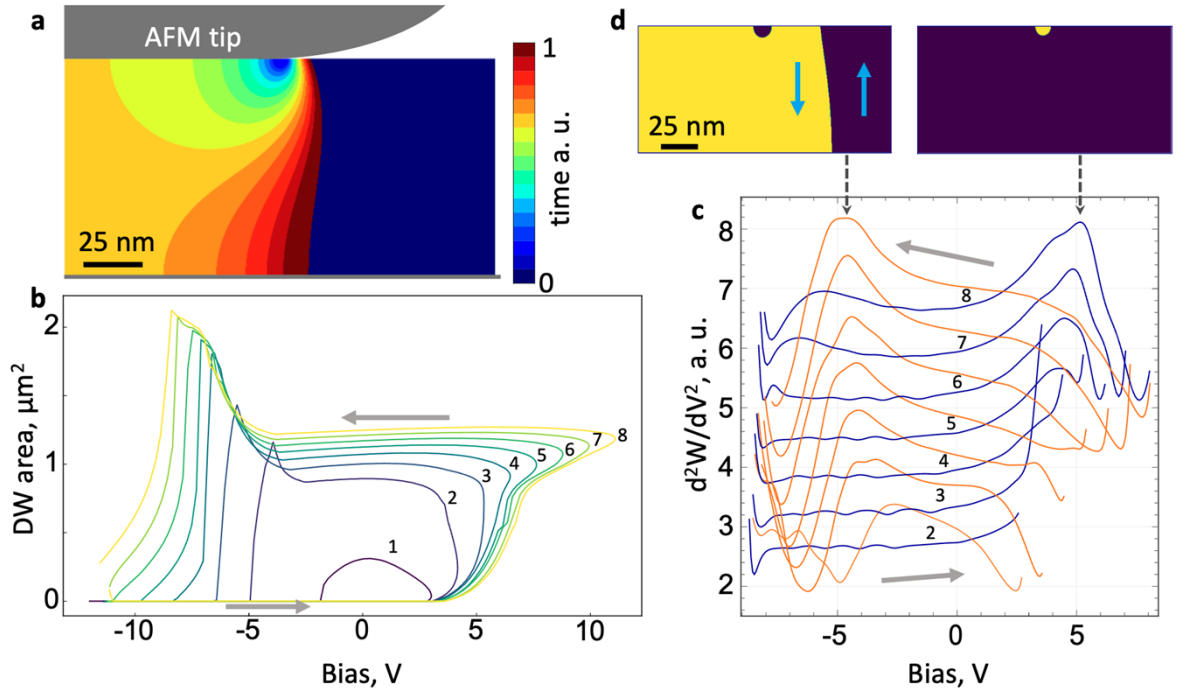

Figure 4. Finite element simulation of partial polarization switching driven by FORC bias waveform applied to the AFM tip. **a)** Evolution of domain shape evolution with linearly increasing bias; **b)** total area of the domain walls as a function of FORC cycle defined by increasing value of positive turning voltage (cycle numbers are shown in the figure; arrows point to the direction of the voltage cycle); **c)** second derivative of the domain wall energy d^2W/dV^2 for polarization configurations in **b** (the first cycle has been skipped for clarity). **d)** Domain configuration corresponding to peak values d^2W/dV^2 in cycle 8 of (c).

To extend this basic model, we utilized finite-element modelling of domain nucleation and growth, under a realistic-tip model with 100 nm contact radius. Although this contact area may be larger than those typically discussed for AFM tip-sample geometries, in the

experiments we deliberately apply force to the tip in order to create a larger contact area. As seen in **Figure 4a**, in this case the domain nucleation does indeed initiate at the periphery of the contact, where the electric field is largest. Upon growth, the domain does not immediately obtain a cylindrical shape. Instead, it proceeds through stages in which it has the form of half-toroid, then dumbbell-like, and eventually cylindrical (see Supplementary Figure S3 for additional details). As illustrated in **Figure 4b**, this shape progression involves an increase of the domain-wall area in the forward direction of the FORC waveform. However, the domain-wall area does not monotonously decrease in the reverse-switching direction. Instead it proceeds through initial increase of the total area (at ~ -5V) followed by a rapid decrease due to annihilation of the wall and reset to a domain-wall-free volume. This reverse transition is remarkably similar to the microwave conductance observed experimentally (**Figure 2b** and **Figure 3b**). Therefore, finite-element modelling provides one possible scenario for geometric variability of the domain-wall conductance, tied to evolution of domain-wall shape upon nucleation and subsequent growth.

A stronger connection of phase-field modelling to the experiment can be obtained by calculating the capacitance of the AFM junction. To this end, we estimated the capacitance of the volume incorporating the nanodomain via the 2nd derivative of the electrostatic energy (detailed in Supplementary Materials). The dependence of small-signal capacitance on applied voltage calculated in this way (**Figure 4c**) is qualitatively reminiscent of the tunable capacitance-voltage characteristics measured experimentally (**Figure 3b**). According to the model, the capacitance is maximized around +/- 5V (**Figure 4c**). These values correspond to the onset of forward switching (yellow nucleus in **Figure 4d**) and the onset of reverse switching (purple nucleus in **Figure 4d**). This is expected since the most polarizable ferroelectric state is the one where the applied field reduces the co-directed polarization to its minimal value right before the initiation of the polarization switching. As a result, we claim that the capacitance peaks measured experimentally correspond to the threshold voltage of the

initial stage of polarization switching, i.e. nucleation of a new nanodomain of opposite polarization. We can then also explain the peculiar synchronization between the sMIM-G and sMIM-C signals, observed on all the studied regions of the film. In particular, the peak of the sMIM-C signal precedes the peak of the sMIM-G signal in all switching spectra, as exemplified by **Figure 3b** (where the peak voltages in the sMIM-C are systematically smaller than in sMIM-G, see red dashed lines). The domain wall of the fresh nucleus does not traverse the film thickness (**Figure 4a,d**). As the nucleation progresses, the area of the domain wall increases, the capacitance of the junction drops, but the conductance starts to increase particularly when the domain wall traverses the volume of the film and makes contact to the bottom electrode (orange to red colors in **Figure 4a**)**.** Therefore, within this interpretation, the peaks in the sMIM-C and sMIM-G signals essentially mark the onset of nucleation and the peak surface area of the domain wall. Finally, the increase of the peak sMIM-G signal with decreasing thickness also provides support for the basic picture of the domain wall as acting as a conductive filament connecting the top and bottom electrodes. In this case, the conductance of the filament will increase with decreasing film thickness, as is observed in **Figure 3b.** The role of the domain-wall curvature may also be present. However, AFM does not provide a direct estimate of domain wall domain wall curvature. This is an important avenue for future research to better understand the possible role of wall morphology and disorder in modulation of conductance [43].

3. Conclusions

To summarize, we have observed tunable microwave conductance associated with ferroelectric switching in a nanoscale contact geometry. The physical mechanism of tunable conductance is traced to the motion of the domain wall through the contact area, and the concomitant increase of the domain wall length in the contact. Nucleation and growth of

nanodomains remains qualitatively similar from 25 nm to 100 nm film thickness of ~25 nm. Such tunable junctions may provide an effective embodiment for neuromorphic circuitry, that maintains highly resistive properties desired for ferroelectric switching, while allowing for tunable electronic read-out of the ferroelectric state. More generally, there will be additional contributions to tunable conductance arising from finite domain tilt or domain wall roughness. Such effects can feasibly be observed in thicker regions of the film where half-prolate domain nuclei with distinct domain wall curvature will be long-lived. Meanwhile, simultaneous piezoelectric and microwave conductance of growing nanodomains sheds new light on the nucleation and growth mechanisms, ultimately enabling new insight into motion of domain walls and the interaction of domain walls with the defects and interfaces.

4. Methods

Thin film fabrication. Single-layer $PbZr_{0.2}Ti_{0.8}O_3$ thin films were synthesized using pulsed-laser deposition. The laser was a KrF excimer laser (248 nm, LPX 305, Coherent), in an on-axis geometry with a 60 mm target-to-substrate distance. Films were grown on 001-oriented $SrTiO_3$ single crystals attached to a resistive heater using Ag paint. $SrRuO_3$ bottom electrodes were grown from sintered ceramic targets at 100 mTorr of continuous O_2. at 630 °C, at a fluence of 1.8 J cm^{-2}, and a frequency of 14 Hz. $PbZr_{0.2}Ti_{0.8}O_3$ was grown from a sintered $Pb_{1.1}Zr_{0.2}Ti_{0.8}O_3$ target at 200 mTorr of continuous O_2. at 645 °C, at a fluence of 1.5 J cm^{-2}, and a frequency of 2 Hz, Following growth all films were cooled to room temperature in a static oxygen 760 mTorr environment at 5°C/min.

sMIM/PFM imaging and spectroscopy. sMIM measurements were carried out through use of a ScanWave module (Prime Nano, Inc.) for Asylum MFP-3D atomic force microscope. The sMIM signal is comprised of the two parts of the complex admittance, $Y = G + jB$. Susceptance, B, is given by the capacitance times the applied ac frequency. The ScanWave

module decouples the signal into sMIM-G (conductance) and sMIM-C (capacitance) signals. To calibrate the probe, the procedure of Huber *et al*. was followed [38], with measurements taken on a SiO_2 standard sample. Simultaneous sMIM and PFM were enabled through a bias-tee integrated in the ScanWave module. Images and spectra were collected through the Asylum AFM software. Further details on the sMIM experiment can be found in reference [30].

Finite element modelling. The details of finite element modelling using COMSOL are described in the supplementary information.

Supporting Information
Supporting Information is available from the Wiley Online Library or from the author.

Acknowledgements
Experiments and modelling have been carried out at the Center for Nanophase Materials Sciences, Oak Ridge National Laboratory, which is a DOE Office of Science User Facility. This research was partially supported by the Australian Research Council Centre of Excellence in Future Low-Energy Electronics Technologies (Project No. CE170100039) and funded by the Australian Government. This project was supported in part by an appointment to the Science Education and Workforce Development Programs at Oak Ridge National Laboratory, administered by ORISE through the U.S. Department of Energy Oak Ridge Institute for Science and Education. S.R.B. acknowledges partial funding from the UNSW Science PhD Writing Scholarship and current funding from the Canada First Research Excellence Fund. In part (A.T.), this work was developed within the scope of the project CICECO-Aveiro Institute of Materials, UIDB/50011/2020 & UIDP/50011/2020, financed by national funds through the FCT/MEC and when appropriate co-financed by FEDER under the PT2020 Partnership Agreement. L.W.M. acknowledges support of the National Science Foundation under grant DMR-1708615.
-
We would like to thank Liam Collins and Rama Vasudevan for assistance with the experimental set-up.

Received: ((will be filled in by the editorial staff))
Revised: ((will be filled in by the editorial staff))
Published online: ((will be filled in by the editorial staff))

References

1. Tsymbal, E.Y., and Kohlstedt, H. (2006) Tunneling Across a Ferroelectric. *Science*, **313** (5784), 181–183.
2. Gruverman, A., Wu, D., Lu, H., Wang, Y., Jang, H.W., Folkman, C.M., Zhuravlev, M.Y., Felker, D., Rzchowski, M., Eom, C.B., and Tsymbal, E.Y. (2009) Tunneling Electroresistance Effect in Ferroelectric Tunnel Junctions at the Nanoscale. *Nano Lett*, **9** (10), 3539–3543.
3. Yamada, H., Garcia, V., Fusil, S., Boyn, S., Marinova, M., Gloter, A., Xavier, S., Grollier, J., Jacquet, E., Carrétéro, C., Deranlot, C., Bibes, M., and Barthélémy, A. (2013) Giant Electroresistance of Super-tetragonal BiFeO3-Based Ferroelectric Tunnel Junctions. *ACS Nano*, **7** (6), 5385–5390.
4. Chanthbouala, A., Crassous, A., Garcia, V., Bouzehouane, K., Fusil, S., Moya, X., Allibe, J., Dlubak, B., Grollier, J., Xavier, S., Deranlot, C., Moshar, A., Proksch, R., Mathur, N.D., Bibes, M., and Barthelemy, A. (2012) Solid-state memories based on ferroelectric tunnel junctions. *Nat Nanotechnol*, **7** (2), 101–104.
5. Boyn, S., Grollier, J., Lecerf, G., Xu, B., Locatelli, N., Fusil, S., Girod, S., Carrétéro, C., Garcia, K., Xavier, S., Tomas, J., Bellaiche, L., Bibes, M., Barthélémy, A., Saïghi, S., and Garcia, V. (2017) Learning through ferroelectric domain dynamics in solid-state synapses. *Nat. Commun.*, **8**, 14736.
6. Sharma, P., Zhang, Q., Sando, D., Lei, C.H., Liu, Y., Li, J., Nagarajan, V., and Seidel, J. (2017) Nonvolatile ferroelectric domain wall memory. *Sci. Adv.*, **3** (6).
7. Sharma, P., Sando, D., Zhang, Q., Cheng, X., Prosandeev, S., Bulanadi, R., Prokhorenko, S., Bellaiche, L., Chen, L.-Q., Nagarajan, V., and Seidel, J. (2019) Conformational Domain Wall Switch. *Adv. Funct. Mater.*, **29** (18), 1807523.
8. Lu, H., Tan, Y., McConville, J.P.V., Ahmadi, Z., Wang, B., Conroy, M., Moore, K., Bangert, U., Shield, J.E., Chen, L.-Q., Gregg, J.M., and Gruverman, A. (2019) Electrical Tunability of Domain Wall Conductivity in LiNbO3 Thin Films. *Adv. Mater.*, **0** (0), 1902890.
9. McConville, J.P.V., Lu, H., Wang, B., Tan, Y., Cochard, C., Conroy, M., Moore, K., Harvey, A., Bangert, U., Chen, L.-Q., Gruverman, A., and Gregg, J.M. Ferroelectric Domain Wall Memristor. *Adv. Funct. Mater.*, **n/a** (n/a), 2000109.
10. Aird, A., and Salje, E.K.H. (1998) Sheet superconductivity in twin walls: experimental evidence of WO3-x. *J Phys Condens Matter*, **10** (22), L377.
11. Maksymovych, P., Jesse, S., Yu, P., Ramesh, R., Baddorf, A.P., and Kalinin, S.V. (2009) Polarization Control of Electron Tunneling into Ferroelectric Surfaces. *Science*, **324** (5933), 1421–1425.
12. Farokhipoor, S., and Noheda, B. (2011) Conduction through 71° Domain Walls in BiFeO 3 Thin Films. *Phys. Rev. Lett.*, **107** (12), 127601.
13. Guyonnet, J., Gaponenko, I., Gariglio, S., and Paruch, P. (2011) Conduction at Domain Walls in Insulating Pb(Zr0.2Ti0.8)O3 Thin Films. *Adv Mater*, **23** (45), 5377–5382.
14. Meier, D., Seidel, J., Cano, A., Delaney, K., Kumagai, Y., Mostovoy, M., Spaldin, N.A., Ramesh, R., and Fiebig, M. (2012) Anisotropic conductance at improper ferroelectric domain walls. *Nat Mater*, **11** (4), 284–8.
15. Seidel, J., Martin, L.W., He, Q., Zhan, Q., Chu, Y.H., Rother, A., Hawkridge, M.E., Maksymovych, P., Yu, P., Gajek, M., Balke, N., Kalinin, S.V., Gemming, S., Wang, F., Catalan, G., Scott, J.F., Spaldin, N.A., Orenstein, J., and Ramesh, R. (2009) Conduction at domain walls in oxide multiferroics. *Nat Mater*, **8** (3), 229–34.
16. Vasudevan, R.K., Matsumoto, Y., Cheng, X., Imai, A., Maruyama, S., Xin, H.L., Okatan, M.B., Jesse, S., Kalinin, S.V., and Nagarajan, V. (2014) Deterministic arbitrary switching of polarization in a ferroelectric thin film. *Nat Commun*, **5**, 4971.
17. Morelli, A., Johann, F., Burns, S.R., Douglas, A., and Gregg, J.M. (2016) Deterministic Switching in Bismuth Ferrite Nanoislands. *Nano Lett*, **16** (8), 5228–5234.

18. Leo, N., Bergman, A., Cano, A., Poudel, N., Lorenz, B., Fiebig, M., and Meier, D. (2015) Polarization control at spin-driven ferroelectric domain walls. *Nat Commun*, **6**, 6661.
19. Heron, J.T., Bosse, J.L., He, Q., Gao, Y., Trassin, M., Ye, L., Clarkson, J.D., Wang, C., Liu, J., Salahuddin, S., Ralph, D.C., Schlom, D.G., Iniguez, J., Huey, B.D., and Ramesh, R. (2014) Deterministic switching of ferromagnetism at room temperature using an electric field. *Nature*, **516** (7531), 370–373.
20. Balke, N., Choudhury, S., Jesse, S., Huijben, M., Chu, Y.H., Baddorf, A.P., Chen, L.Q., Ramesh, R., and Kalinin, S.V. (2009) Deterministic control of ferroelastic switching in multiferroic materials. *Nat. Nanotechnol.*, **4** (12), 868–875.
21. Parkin, S.S.P., Hayashi, M., and Thomas, L. (2008) Magnetic Domain-Wall Racetrack Memory. *Science*, **320** (5873), 190–194.
22. Manipatruni, S., Nikonov, D.E., Lin, C.-C., Gosavi, T.A., Liu, H., Prasad, B., Huang, Y.-L., Bonturim, E., Ramesh, R., and Young, I.A. (2019) Scalable energy-efficient magnetoelectric spin–orbit logic. *Nature*, **565** (7737), 35–42.
23. A. Benedek, N., and Birol, T. (2016) 'Ferroelectric' metals reexamined: fundamental mechanisms and design considerations for new materials. *J. Mater. Chem. C*, **4** (18), 4000–4015.
24. Zhou, W.X. (2020) Review on ferroelectric/polar metals. *Jpn J Appl Phys*, 14.
25. Bruno, F.Y., Boyn, S., Fusil, S., Girod, S., Carrétéro, C., Marinova, M., Gloter, A., Xavier, S., Deranlot, C., Bibes, M., Barthélémy, A., and Garcia, V. (2016) Millionfold Resistance Change in Ferroelectric Tunnel Junctions Based on Nickelate Electrodes. *Adv. Electron. Mater.*, **2** (3), 1500245.
26. Chaudhary, P., Lu, H., Lipatov, A., Ahmadi, Z., McConville, J.P.V., Sokolov, A., Shield, J.E., Sinitskii, A., Gregg, J.M., and Gruverman, A. (2020) Low-Voltage Domain-Wall LiNbO3 Memristors. *Nano Lett.*
27. Sluka, T., Tagantsev, A.K., Bednyakov, P., and Setter, N. (2013) Free-electron gas at charged domain walls in insulating BaTiO(3). *Nat Commun*, **4**, 1808.
28. Fujioka, J., Doi, A., Okuyama, D., Morikawa, D., Arima, T., Okada, K.N., Kaneko, Y., Fukuda, T., Uchiyama, H., Ishikawa, D., Baron, A.Q.R., Kato, K., Takata, M., and Tokura, Y. (2015) Ferroelectric-like metallic state in electron doped BaTiO 3. *Sci. Rep.*, **5** (1), 13207.
29. Wu, X., Petralanda, U., Zheng, L., Ren, Y., Hu, R., Cheong, S.-W., Artyukhin, S., and Lai, K. (2017) Low-energy structural dynamics of ferroelectric domain walls in hexagonal rare-earth manganites. *Sci. Adv.*, **3** (5).
30. Tselev, A., Yu, P., Cao, Y., Dedon, L.R., Martin, L.W., Kalinin, S.V., and Maksymovych, P. (2016) Microwave a.c. conductivity of domain walls in ferroelectric thin films. *Nat. Commun.*, **7**, 11630.
31. Huang, Y.-L., Zheng, L., Chen, P., Cheng, X., Hsu, S.-L., Yang, T., Wu, X., Ponet, L., Ramesh, R., Chen, L.-Q., Artyukhin, S., Chu, Y.-H., and Lai, K. (2020) Unexpected Giant Microwave Conductivity in a Nominally Silent BiFeO3 Domain Wall. *Adv. Mater.*, **32** (9), 1905132.
32. Cheng, S., Fan, Z., Rao, J., Hong, L., Huang, Q., Tao, R., Hou, Z., Qin, M., Zeng, M., Lu, X., Zhou, G., Yuan, G., Gao, X., and Liu, J.-M. (2020) Highly Controllable and Silicon-Compatible Ferroelectric Photovoltaic Synapses for Neuromorphic Computing. *iScience*, **23** (12), 101874.
33. Damodaran, A.R., Pandya, S., Agar, J.C., Cao, Y., Vasudevan, R.K., Xu, R., Saremi, S., Li, Q., Kim, J., McCarter, M.R., Dedon, L.R., Angsten, T., Balke, N., Jesse, S., Asta, M., Kalinin, S.V., and Martin, L.W. (2017) Three-State Ferroelastic Switching and Large Electromechanical Responses in PbTiO3 Thin Films. *Adv. Mater.*, **29** (37), 1702069.
34. Agar, J.C., Mangalam, R.V.K., Damodaran, A.R., Velarde, G., Karthik, J., Okatan, M.B., Chen, Z.H., Jesse, S., Balke, N., Kalinin, S.V., and Martin, L.W. (2014) Tuning

Susceptibility via Misfit Strain in Relaxed Morphotropic Phase Boundary PbZr1-xTixO3 Epitaxial Thin Films. *Adv. Mater. Interfaces*, **1** (5), 1400098.
35. Ievlev, A.V., Marius, C., Donovan, N.L., Joshua, C.A., Gabriel, A.V., Lane, W.M., Sergei, V.K., Petro, M., and Olga, S.O. (2018) Subtractive fabrication of ferroelectric thin films with precisely controlled thickness. *Nanotechnology*, **29** (15), 155302.
36. Ramesh, R. (2016) Ultralow energy electric field control of magnetism: can we get to 1 AttoJoule/bit? (Conference Presentation). *Spintron. IX*, **9931**, 99312K.
37. Wu, X., Du, K., Zheng, L., Wu, D., Cheong, S.-W., and Lai, K. (8) Microwave conductivity of ferroelectric domains and domain walls in a hexagonal rare-earth ferrite. *Phys. Rev. B*, **98** (8), 081409.
38. Huber, H.P., Moertelmaier, M., Wallis, T.M., Chiang, C.J., Hochleitner, M., Imtiaz, A., Oh, Y.J., Schilcher, K., Dieudonne, M., Smoliner, J., Hinterdorfer, P., Rosner, S.J., Tanbakuchi, H., Kabos, P., and Kienberger, F. (2010) Calibrated nanoscale capacitance measurements using a scanning microwave microscope. *Rev. Sci. Instrum.*, **81** (11), 113701.
39. Lai, K., Kundhikanjana, W., Kelly, M.A., and Shen, Z.-X. (2011) Nanoscale microwave microscopy using shielded cantilever probes. *Appl. Nanosci.*, **1** (1), 13–18.
40. Shin, J., Nascimento, V.B., Geneste, G., Rundgren, J., Plummer, E.W., Dkhil, B., Kalinin, S.V., and Baddorf, A.P. (2009) Atomistic Screening Mechanism of Ferroelectric Surfaces: An In Situ Study of the Polar Phase in Ultrathin BaTiO3 Films Exposed to H2O. *Nano Lett.*, **9** (11), 3720–3725.
41. Maksymovych, P., Seidel, J., Chu, Y.H., Wu, P., Baddorf, A.P., Chen, L.Q., Kalinin, S.V., and Ramesh, R. (2011) Dynamic conductivity of ferroelectric domain walls in BiFeO(3). *Nano Lett*, **11** (5), 1906–12.
42. Eliseev, E.A., Morozovska, A.N., Svechnikov, G.S., Maksymovych, P., and Kalinin, S.V. (December 1) Domain wall conduction in multiaxial ferroelectrics. *Phys. Rev. B*, **85** (4), 045312.
43. Li, L., Jokisaari, J.R., Zhang, Y., Cheng, X., Yan, X., Heikes, C., Lin, Q., Gadre, C., Schlom, D.G., Chen, L.-Q., and Pan, X. (2018) Control of Domain Structures in Multiferroic Thin Films through Defect Engineering. *Adv. Mater.*, **30** (38), 1802737.
44. Morozovska, A.N., Ievlev, A.V., Obukhovskii, V.V., Fomichov, Y., Varenyk, O.V., Shur, V.Ya., Kalinin, S.V., and Eliseev, E.A. (2016) Self-consistent theory of nanodomain formation on nonpolar surfaces of ferroelectrics. *Phys. Rev. B*, **93** (16), 165439.
45. Ievlev, A.V., Alikin, D.O., Morozovska, A.N., Varenyk, O.V., Eliseev, E.A., Kholkin, A.L., Shur, V.Ya., and Kalinin, S.V. (2015) Symmetry Breaking and Electrical Frustration during Tip-Induced Polarization Switching in the Nonpolar Cut of Lithium Niobate Single Crystals. *ACS Nano*, **9** (1), 769–777.

Tunable microwave conductance is induced by ferroelectric switching in lead zirconate titanate ($PbZr_{0.2}Ti_{0.8}O_3$). Through subtractive milling, statistical analysis and finite element modelling, we have elucidated the mechanism of tunable microwave conductance as related to the domain wall density under the scanning probe. The results are promising for ferroelectric memristors.

S.R. Burns*, A. Tselev, A.V. Ievlev, J.C. Agar, L.W. Martin, S.V. Kalinin, D. Sando, P. Maksymovych*

Tunable microwave conductance of nanodomains in ferroelectric PbZr0.2Ti0.8O3 thin film

ToC figure

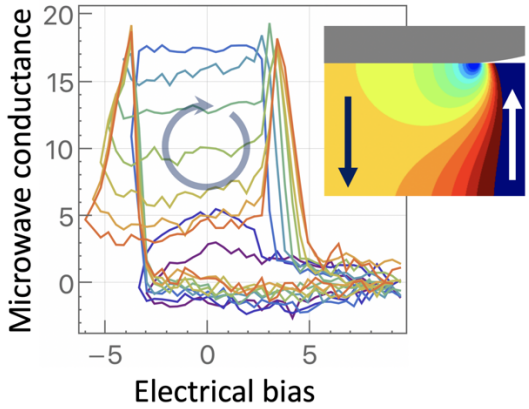

Supporting Information

Tunable microwave conductance of nanodomains in ferroelectric PbZr0.2Ti0.8O3 thin film

Stuart R. Burns, Alexander Tselev, Anton V. Ievlev, Joshua C. Agar, Lane W. Martin, Sergei V. Kalinin, Daniel Sando, Petro Maksymovych**

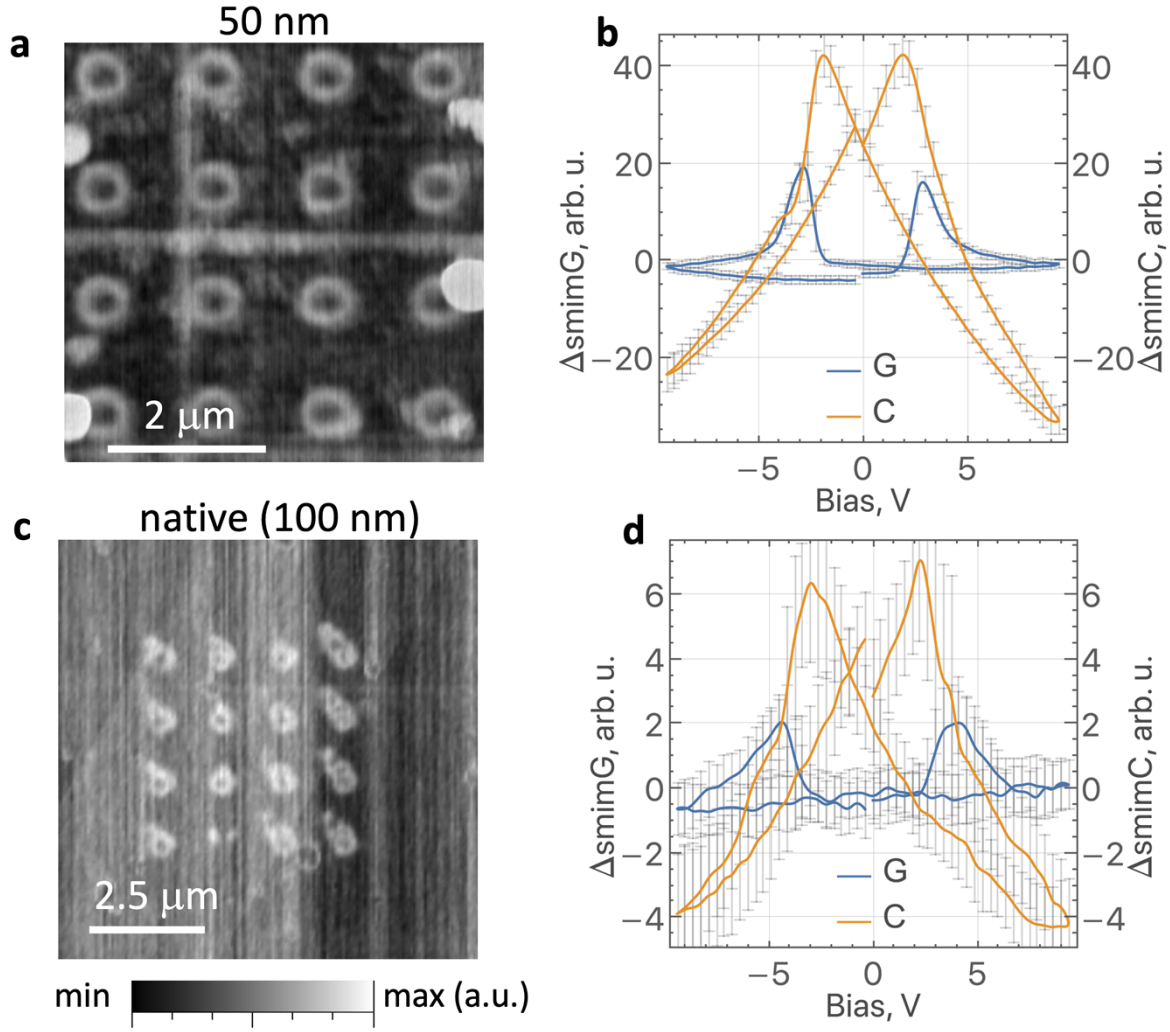

Figure S1. Tunable microwave conductance in regions of the PZT film etched down to 50 nm and the native (100 nm thickness). The information shown is the same as in **Figure 3a,b**.

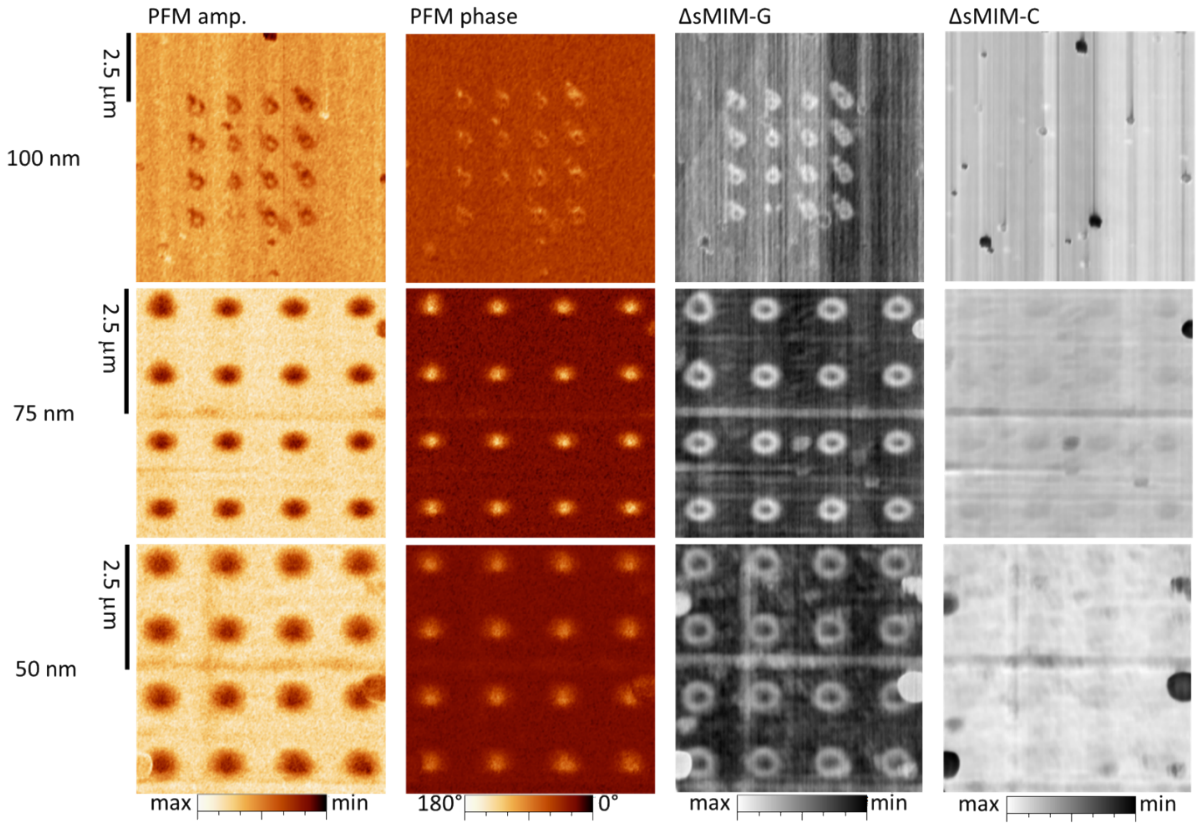

Figure S2. PFM amplitude, PFM phase, sMIM conductance and sMIM capacitance images of point-poled arrays in three regions of the PZT film after ToF-SIMS milling (namely, 50 nm thick, 75 nm thick and 100 nm thick regions). These data are quantitatively presented in **Figure 4a** and **b**.

Finite element modelling

To understand behaviour of spontaneous polarization during electric field application, we carried out finite element simulations in the framework of the Landau-Ginzburg-Devonshire (LGD) theory using COMSOL Multiphysics 4.4 software package. We considered two-layered system formed by air layer and ferroelectric of thickness L = 100 nm in 2D axisymmetric geometry, separated by surface z = 0. Local distribution of z-component of ferroelectric polarization $P_z(r,z)$ was calculated using the dimensionless time-dependent LGD equation (eq. (1)). [44,45]

$$\frac{\partial \widetilde{P}_z}{\partial \tau} - \widetilde{P}_z + \widetilde{P}_z{}^3 - R_c\left(\frac{1}{r}\frac{\partial}{\partial r}\left(r\frac{\partial \widetilde{P}_z}{\partial r}\right) + \frac{\partial^2 \widetilde{P}_z}{\partial z^2}\right) = \widetilde{E}_z \qquad (1)$$

where $\widetilde{P}_z = {}^{P_z}/_{P_s}$ is ferroelectrc polarization normalized by the spontaneous polarization P_s = 0.75 C/m^2; $\widetilde{E}_z = {}^{E_z}/_{E_c}$ is the external electric field $E_z(r,z)$ normalized by the coercive field $E_c = 5\times10^7$ V/m; $\tau = {}^{t}/_{t_0}$ is the dimensionless time defined as a time t normalized by a characteristic time $t_0 = \frac{\Gamma}{\alpha}$, where Γ is the kinetic Khalatnikov coefficient, and $\alpha = 1.77\times10^8$ m/F is the generalized dielectric stiffness; R_c is the correlation length, which is about 1 nm at room temperature. In the simulation, the polarization is assumed to be perfectly screened, which is ensured by boundary charges on the ferroelectric surface with a surface density σ

$(r,z=0) = -P_Z(r,z=0)$. This is also complemented by boundary conditions $\widetilde{P}_z(r\to\infty) = 1$ and $\frac{\partial \widetilde{P}_z}{\partial r}(r\to\infty) = 0$.

To define quasi-stationary electric field E_z in eq. (1), corresponding electrostatic potential φ is introduced as $\boldsymbol{E} = -\nabla\varphi$. The potential φ satisfies the electrostatic Laplace equation. In the ambient semispace, 0 < z < +∞ (excluding tip volume):

$$\frac{1}{r}\frac{\partial}{\partial r}\left(r\frac{\partial \varphi_d}{\partial r}\right) + \frac{\partial^2 \varphi_d}{\partial r^2} = 0. \qquad (2)$$

The subscript d denotes ambient. In the following, the subscripts and superscripts d and f refer to the ambient and ferroelectric, respectively. The AFM tip is represented by a cut sphere with radius R_{tip} = 20 nm and small flat contact plate with a radius r_{cont} = 5 nm. Applied bias is introduced as the potential of the tip equipotential surface $\varphi_d|_{tip} = U(t)$. The boundary conditions at the interface z = 0 are continuous potential across the boundaries between the ferroelectric and ambient $\varphi_d(r,z=0) = \varphi_f(r,z=0)$ and continuous normal component of the displacement field: $D_z^d - D_z^f\big|_{z=0} = 0$, where $D_z^d = -\varepsilon_0\varepsilon_d\left(\partial\varphi_d/\partial z\right)$ and $D_z^f = -\varepsilon_0\varepsilon_{33}^f\left(\partial\varphi_f/\partial z\right)$.

Maxwell equation $\mathrm{div}\boldsymbol{D} = 0$ along with the constitutive relations $D_r = \varepsilon_0\varepsilon_{11}^f E_r$, and $D_z = -\varepsilon_0\varepsilon_{33}^f E_z + P_z$ yields the anisotropic Poisson equation inside the ferroelectric-semiconductor layer -L < z < 0. Including polarization gradient, the potential distribution within ferroelectric is:

$$\varepsilon_0\left(\varepsilon_{11}^f\frac{1}{r}\frac{\partial}{\partial r}\left(r\frac{\partial\varphi_f}{\partial r}\right) + \varepsilon_{33}^b\frac{\partial^2\varphi_f}{\partial z^2}\right) = \frac{\partial P_z}{\partial z}. \qquad (3)$$

Here ε_0 = 8.85×10^{-12} F/m is the universal dielectric constant, $\varepsilon_{33}^b \approx 5$ is the background dielectric permittivity of the ferroelectric, and $\varepsilon_{11}^f \approx 75$. The grounded bottom electrode was accounted for by a zero-potential boundary condition $\varphi_f(r,z=-L) = 0$.

Switching was achieved by applying a FORC waveform shown in figure 1b. Evolution of the resulted domain in linearly increasing bias is shown below.

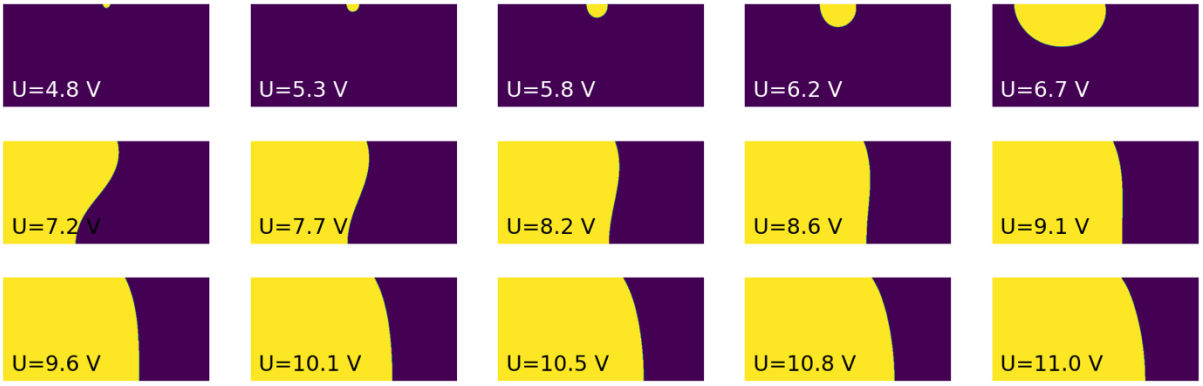

Figure S3. COMSOL simulated evolution of the domain geometry in linearly increasing bias applied to AFM tip.

To compare finite element results to experiment, we calculated the second derivative of the electrostatic energy stored in the system, W (Figure S3a), over the applied bias, d^2W/dV^2. The use of d^2W/dV^2 in place of the small-signal (differential) capacitance measured in the sMIM experiments requires extra explanation. The output our finite-elements modelling includes the electrostatic energy of the probe-sample system, but not its capacitance where the ferroelectric is a material with non-linear, field-dependent, dielectric permittivity. We note

that the capacitance C of a linear capacitor (with a dielectric permittivity independent of the electric field strength) is constant and can be obtained by differentiating twice the energy W over the applied bias V: $C = d^2W/dV^2$.

To obtain an expression for processing of the results of the numeric modelling, we start with the expression for the capacitor energy W through its charge Q and voltage V noting that the quantity detected as capacitance in the sMIM experiments is the differential, small voltage amplitude, capacitance, i.e., $C_{ac} = dQ/dV$:

$$W = \frac{QV}{2} . \tag{4}$$

The first derivative of the energy is:

$$\frac{dW}{dV} = \frac{1}{2}Q + \frac{1}{2}V\frac{dQ}{dV} . \tag{5}$$

The differential capacitance is now in the second term in the right-hand side. Re-writing further:

$$\frac{1}{V}\frac{dW}{dV} = \frac{1}{2}\frac{Q}{V} + \frac{1}{2}\frac{dQ}{dV} = \frac{1}{2}C_{ch} + \frac{1}{2}C_{ac}, \tag{6}$$

where C_{ch} is the chordal capacitance. This expression is unsuitable to work with discrete datasets resulting from the numerical calculations because of the singular behaviour of the left-hand side at V=0 due to calculation uncertainty and inevitable offsets from zero values at V=0 in the calculated data. In turn, the second derivative of the energy remains in a limited range in the numerical processing near V=0, and the left-hand side of eq. (6) can be expressed through it. We can use the expression of the energy through capacitance and voltage to get the necessary relations:

$$W = \frac{C(V)V^2}{2}. \tag{7}$$

$C(V)$ here is equivalent to the chordal capacitance C_{ch}. For the first derivative of W ($W' = dW/dV$):

$$W' = \frac{1}{2}C'V^2 + C(V)V = (\frac{1}{2}C'V + C(V))V \tag{8}$$

and

$$\frac{1}{V}W' = \frac{1}{2}C'V + C(V). \tag{9}$$

For the second derivative,

$$W'' = \frac{1}{2}C''V^2 + 2C'V + C(V) \approx 2C'V + C(V) \tag{10}$$

(if the dielectric nonlinearity is small enough, the term with C'' can be neglected). Using eqs. (9) and (10), we can eliminate the term with C' and write:

$$\frac{1}{V}W' = \frac{1}{4}W'' + \frac{3}{4}C(V) = \frac{1}{4}W'' + \frac{3}{4}C_{ch}. \tag{11}$$

Equating right-hand sides of eqs. (6) and (11), we get:

$$\frac{1}{4}W'' + \frac{3}{4}C_{ch} = \frac{1}{2}C_{ch} + \frac{1}{2}C_{ac}, \tag{12}$$

which yields:

$$C_{ac} = \frac{1}{2}W'' + \frac{1}{2}C_{ch} \tag{13}$$

or

$$C_{ac} = \frac{1}{2}W'' + \frac{W}{V^2}. \tag{14}$$

This expression gives a correct result in the case when there is no nonlinearity and the capacitance does not depend on V. The second term in the right-hand side of eq. (14) is approximately constant. This is easy to see if we represent W through the second derivative and integrals of the type:

$$W = \int_0^V \left(\int_0^V W'' dV \right) dV \tag{15}$$

Equation (15) is valid for positive bias voltages. For negative voltages, similar integration can be used. An isolated peak in the second derivative above a constant value, as is in Figure 5d of the main text, will give only a small addition to the result of the first integration in eq. (15) compared to the integration of a constant value corresponding to a linear capacitor with a voltage-independent capacitance. Therefore, from eq. (14), W'' reveals the tunability peaks and, hence, was used in our work to analyse the numerical modelling results in the main text. Calculation results for the non-linear dielectric is qualitatively similar to the experimental observations, with peaks in W'' corresponding to the onset of domain nucleation (Figure 5c,d). For a linear dielectric, $W'' = C$, as we have directly verified by FEM calculation in a similar model, as shown in Figure S3c.

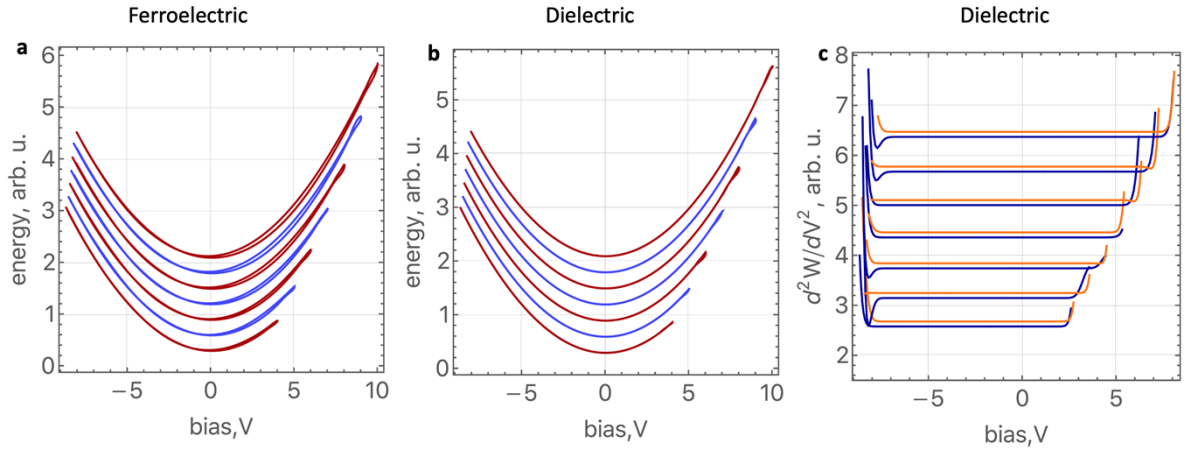

Figure S4. Calculated electrostatic energy in the probe-sample system for a FORC electric bias waveform applied to a 100 nm contact radius incorporating: **a)** a ferroelectric with switchable spontaneous polarization; **b)** identical geometry but a linear dielectric with no spontaneous polarization. Individual curves correspond to each FORC cycle are offset for clarity. **c)** Second derivative of electrostatic energy wrt to applied bias (d^2W/dV^2) was calculated for a linear dielectric shows no field-induced variation as expected, in stark contrast to the behaviour of the ferroelectric in Figure 5d of the main text. All curves are offset for clarify. The "tails" are a numerical artefact due to numerical differentiation of dependences in (b) near turning voltages.